Nanoscale

PAPER

View Article Online
View Journal | View Issue

Check for updates

Cite this: *Nanoscale*, 2025, **17**, 8880

Enhancing photocatalytic performance of F-doped TiO_2 through the integration of small amounts of a quinoline-based covalent triazine framework†

Alicia Moya,[a] Miguel Sánchez-Fuente,[a] Marta Linde,[a] Víctor Cepa-López,[a] Isabel del Hierro,[b,c] Miguel Díaz-Sánchez,*[b] Santiago Gómez-Ruiz*[b,c] and Rubén Mas-Ballesté*[a,d]

Received 20th December 2024,
Accepted 3rd March 2025

DOI: 10.1039/d4nr05363j

rsc.li/nanoscale

We present the design and synthesis of a new quinoline-based covalent triazine framework (**Quin-CTF**) that combines two photoactive fragments within its structure (triazine and quinoline moieties). By hybridizing this CTF material with fluorine-doped titanium dioxide (**F-TiO$_2$**), we prepared and characterized photocatalysts with enhanced performance that leverage the synergy between the two components for pollutant photodegradation in water. This **F-TiO$_2$@CTF** hybrid system was evaluated for the photocatalytic degradation of methylene blue dye and a pharmaceutical compound such as ciprofloxacin as model water pollutants. The hybrid materials containing small amounts of CTF (0.5, 1, and 2 wt%) achieved remarkable photodegradation efficiencies, significantly outperforming their individual counterparts. The reactive oxidant species (ROS) involved in such processes catalyzed by **F-TiO$_2$** are different from those involved when pristine **Quin-CTF** or their hybrid materials are used. Furthermore, the hybrid materials demonstrated reusability, preserving high photocatalytic activity over multiple cycles. This work, therefore, highlights a promising strategy for designing cost-effective and eco-friendly photocatalytic systems *via* the incorporation of a small amount of CTF-based systems in a cheap material such as titanium dioxide, offering a sustainable and effective solution for mitigating water pollution.

Introduction

Developing sustainable technologies for mitigating water pollution has become an urgent social need. A significant challenge in this field is the effective removal of emerging contaminants, many of which resist conventional wastewater treatments.[1] The persistence of these pollutants poses severe threats to aquatic ecosystems, public health, and biodiversity, highlighting the requirement for advanced and efficient remediation technologies. Among the promising strategies, photocatalytic degradation has gained attention for its ability to remove organic pollutants in water through advanced oxidation processes (AOP).[2,3] Titanium dioxide (TiO_2) has emerged as a leading photocatalyst due to its low cost, high chemical stability, non-toxicity, and resistance to photocorrosion.[4–6] Nevertheless, the photocatalytic performance of these materials remains limited by specific morphological and electronic factors.[7] This limitation emphasizes the need for further research to improve their functionality by exploiting other wavelengths of activating light, optimizing degradation pathways, and extending their applicability to a broader spectrum of pollutants.

To extend the versatility of this inorganic photocatalyst, various strategies have been explored to modify its photophysical properties. Among those, elemental doping, particularly with fluorine, has proven effective by increasing the surface area, reducing the band gap, and promoting the migration of photogenerated charge carriers.[8,9] This leads to the formation of Ti^{3+} ions and oxygen vacancies, which minimize the electron–hole recombination and enhance photocatalytic performance.[10–15] Additionally, fluorine doping induces the formation of highly reactive {001} facets, increasing O vacancies and boosting photoactivity.[16–18] In a further

---

[a] Departamento de Química Inorgánica, Facultad de Ciencias, Calle Francisco Tomás y Valiente, 7, Universidad Autónoma de Madrid, Ciudad Universitaria de Cantoblanco, 28049 Madrid, Spain. E-mail: ruben.mas@uam.es

[b] COMET-NANO Group, Departamento de Biología y Geología, Física y Química Inorgánica, E.S.C.E.T., Universidad Rey Juan Carlos, Calle Tulipán s/n, E-28933 Móstoles, Madrid, Spain. E-mail: miguel.diaz@urjc.es, santiago.gomez@urjc.es

[c] Instituto de Investigación de Tecnologías para la Sostenibilidad, Universidad Rey Juan Carlos, Calle Tulipán s/n, 28933 Móstoles, Madrid, Spain

[d] Institute for Advanced Research in Chemical Sciences (IAdChem), Facultad de Ciencias, Calle Francisco Tomás y Valiente, 7, Universidad Autónoma de Madrid, Ciudad Universitaria de Cantoblanco, 28049 Madrid, Spain

† Electronic supplementary information (ESI) available. See DOI: https://doi.org/10.1039/d4nr05363j

twist on surface modification of TiO_2, carbon species incorporation resulted in decreasing charge recombination and reducing the band gap.[19,20]

Carbon-based and related organic reticular materials offer a plethora of structural motifs to enhance the photocatalytic activity of TiO_2 by reducing charge recombination and lowering the band gap energy. Thus, covalent organic frameworks (COFs), and covalent triazine frameworks (CTFs) have appeared as good candidates for exploring innovative engineered materials due to their high surface porosity and robust electronic properties.[21–23] For example, TiO_2@COF materials with COF contents ranging between 20 and 40 wt% have been used for photooxidation of benzyl alcohol, reporting conversions higher than those of their pristine materials.[24] Furthermore, another TiO_2@COF material with a high load of COF (>90%) has also demonstrated excellent photocatalytic conversion and selectivity for the oxidative coupling of benzylamines to *N*-benzyl-1-phenylmethanimine.[25] Among these types of hybrid materials, TiO_2–CTF hybrids offer many underexplored possibilities. CTF materials are composed of solely organic structures that are assembled through the formation of the 1,3,5-triazine ring, that display a variety of photocatalytic properties.[26] Thus, fluorine-doped TiO_2 was combined with CTFs leading to $TiO_{2-X}F_X$/CTFs hybrids with 15–50 wt% of the CTF material and were used for photocatalytic degradation of carbamazepine, raising 5.5 times higher activity than pure $TiO_{2-X}F_X$.[27] These hybrids extend the absorption towards the visible range, prevent photocarrier recombination, and provide more reactive active sites. Despite promising initial results, research on these hybrid materials remains limited to a few examples where high-weight fractions of the organic material have been employed. However, cost-effective solutions should imply a reduction in the fraction of the organic material to increase their sustainability, and this might be achieved by designing hybrid systems with TiO_2 as the major component. This underexplored area holds immense potential for novel materials with synergistic structural and electronic properties, offering robust solutions for water treatment and environmental remediation.

In this work, we report a novel quinoline-based covalent triazine framework (**Quin-CTF**) with photocatalytic activity arising from the combination of N-rich moieties (quinoline and triazine) within a highly conjugated framework, enabling efficient electronic delocalization.[28,29] This work explores the hybridization of fluorine-doped TiO_2 (**F-TiO$_2$**) structures with small amounts (from 0.5 to 2 wt%) of **Quin-CTF** to form **F-TiO$_2$@CTF** hybrids, further enhancing photocatalytic performance of titanium dioxide materials. This strategy leads to the cost-effectiveness of TiO_2 as the primary component and the functional advantages of its hybridization with **Quin-CTF**. The resulting hybrid material demonstrates improved photocatalytic properties for degrading model pollutants in water such as methylene blue dye (MB) and the pharmaceutical compound ciprofloxacin (CP). Overall, this work contributes to the continued research to pave the way for efficient, low-cost, sustainable, and eco-friendly TiO_2-based photocatalytic systems, contributing to a cleaner and healthier environment.

Experimental section

Synthesis of organic compounds

Synthesis of 6-diiodo-4-phenylquinoline (Quin-I). 4-Iodoaniline (631 mg, 2.88 mmol), 4-iodobenzaldehyde (668 mg, 2.88 mmol), phenylacetylene (302 μL, 294 mg, 2.88 mmol), bromobenzene (8 mL) and scandium trifluoromethanesulfonate ($Sc(OTf)_3$, 142 mg, 0.29 mmol, 10 mol%) were introduced into a sealed tube with a magnetic stir bar. The reaction was heated to 120 °C for 48 hours. After two days, the solvent was evaporated under reduced pressure. The compound was then purified *via* column chromatography using a 1 : 1 mixture of dichloromethane and cyclohexane. Finally, it was washed with cold acetone and dried under vacuum, affording **Quin-I** (see Scheme 1) as a pale-yellow solid in 40% yield. ^1H NMR (300 MHz, $CDCl_3$) δ 8.24 (d, J = 1.8 Hz, 1H), 8.00–7.89 (m, 4H), 7.88–7.82 (m, 2H), 7.76 (s, 1H), 7.64–7.47 (m, 5H). ^{13}C-RMN: ($CDCl_3$, 75 MHz, ppm) δ 156.12, 148.47, 147.69, 138.57, 138.07, 137.56, 134.51, 131.76, 129.47, 129.24, 128.91, 128.86, 127.66, 119.38, 96.37, 92.48 (Fig. S1 and S2†).

Synthesis of 4-(6-(4-isocyanophenyl)-4-phenylquinolin-2-yl) benzo-nitrile (Quin-CN). 6-Diiodo-4-phenylquinoline (1.2 g, 2.25 mmol), 4-cyanophenylboronic acid (727 mg, 4.95 mmol), potassium carbonate (1.37 g, 9.93 mmol), and $Pd(PPh_3)_4$ (260 mg, 0.225 mmol, 10 mol%) were added to a Schlenk flask equipped with a stir bar and subjected to three vacuum–argon cycles. Then, 50 mL of a 5 : 1 mixture of tetrahydrofuran and water previously degassed with argon was introduced into the flask. The reaction was heated to 80 °C for 48 hours. After the reaction was accomplished, the solid in the crude was washed with methanol and diethyl ether, isolating the product **Quin-CN** (see Scheme 1) as a white powder in a 64% yield. The following signals confirmed the formation of this product: ^1H NMR (300 MHz, $CDCl_3$) δ 8.37 (d, J = 8.5 Hz, 3H), 8.12 (d, J = 2.0 Hz, 1H), 8.01 (dd, J = 8.8, 2.1 Hz, 1H), 7.92 (s, 1H), 7.81–7.70 (m, 10H), 7.66–7.55 (m, 5H). ^{13}C NMR ($CDCl_3$, 75 MHz) δ 156.5, 149.9, 148.6, 145.0, 144.9, 140.3, 139.5, 137.9, 137.2, 132.7, 131.1, 129.5, 128.9, 128.9, 128.8, 128.4, 128.0, 127.8, 126.1, 124.3, 119.9, 118.9, 118.8, 111.3, 111.3 (Fig. S3 and S4†).

Synthesis of Quin-CTF. In a 50 mL round-bottom flask, 123 mg of the building block **Quin-CN** was added to 6.35 mL of dichloromethane (DCM), followed by the dropwise addition of 0.5 mL of trifluoromethanesulfonic acid under an ice bath, and the reaction mixture was stirred at room temperature for 12 hours. Then, 20 mL of a 1 : 1 ethanol/water mixture was added dropwise over the mixture under an ice bath. The resulting solid was centrifuged and washed with a 1 : 1 ethanol/water mixture until a neutral pH was reached. Finally, the solid was washed with NEt_3, MeOH, DCM, and acetone, obtaining the yellow **Quin-CTF** material in a 70% yield.

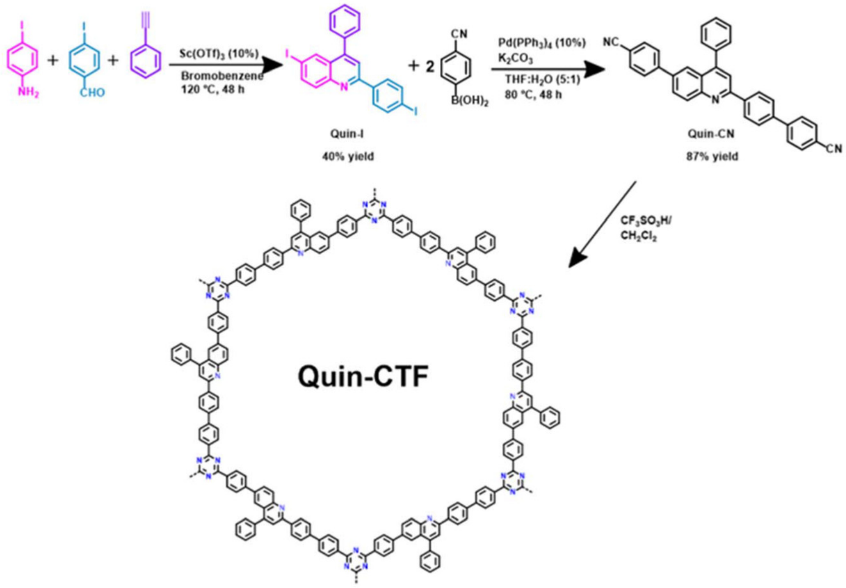

Scheme 1 Synthetic procedure to obtain the new material **Quin-CTF** through the formation of (1) **Quin-I** through Povarov reaction, (2) **Quin-CN** through Suzuki–Miyaura cross-coupling reaction, and (3) **Quin-CTF** material through cyclotrimerization in acid media.

Synthesis of F-TiO_2 nano-sized aggregates

The nano-sized aggregates of fluorine-doped titanium dioxide (**F-TiO_2**) were synthesized *via* sol–gel method optimized by our research group.[19,30] The synthesis started with the preparation of a solution containing 30 mL of titanium isopropoxide (TTIP) dissolved in 75 mL of 2-propanol. Subsequently, a second solution was obtained by dissolving 0.88 g of sodium fluoride (NaF) in 75 mL of ultrapure water, resulting in a fluorine doping mass ratio of 5%. Both the TTIP solution and the NaF solution were added dropwise to 500 mL of nitric acid solution in ultrapure water, maintaining pH 2. The mixture was subjected to vigorous stirring at room temperature for 16 hours. The resulting white precipitate was isolated by filtration and washing with ultrapure water and ethanol to remove any impurities. The collected material was dried at 80 °C overnight. After drying, the samples were ground and calcined in air at 500 °C using a Nabertherm LT-3/12 1200 furnace for 16 hours at a heating rate of 0.8 °C min^{-1}.

Synthesis of F-TiO_2@CTF hybrid materials

The incorporation of **Quin-CTF** into fluorine-doped titanium dioxide (**F-TiO_2**) was conducted at varying mass ratios of CTF with respect to the oxide (0.5, 1, and 2 wt%). To facilitate this process, the two pristine materials were combined in a round-bottom flask containing 100 mL of ethanol, which was subsequently sealed with a Teflon stopper. The dispersion was subjected to sonication for 1 hour to ensure homogeneity, followed by magnetic stirring at room temperature for 48 hours. The resulting hybrid materials were then isolated by centrifugation and washed thoroughly with water and ethanol. The final products were dried in an oven at 80 °C overnight, resulting in the photocatalysts denoted as **F-TiO_2@0.5CTF**, **F-TiO_2@1CTF**, and **F-TiO_2@2CTF**. All hybrid materials were evaluated in photocatalytic studies and compared with pristine **F-TiO_2** and **Quin-CTF** for performance assessment.

Evaluation of the photocatalytic activity of the materials obtained

To assess the photocatalytic activity of the hybrid materials (**F-TiO_2@0.5CTF**, **F-TiO_2@1CTF**, and **F-TiO_2@2CTF**) as well as the individual pristine components (**F-TiO_2** and **Quin-CTF**), 2.5 mg of each material was introduced in a vial which contains a magnetic bar and 10 mL of a solution containing either 10 ppm of MB or 20 ppm of CP. The suspensions were subjected to ultrasound treatment for 2 minutes to ensure adequate dispersion of the photocatalyst, followed by 2 minutes of oxygen purge to improve the reaction environment. Subsequently, the suspensions were stirred in the dark for 1 hour to obtain complete saturation of the pollutant adsorption on the photocatalyst surfaces and reach the adsorption–desorption equilibrium. The photodegradation reaction time was 50 minutes for MB and 30 minutes for CP. In the photodegradation kinetic experiments, the reaction products were determined every 10 minutes for MB and 5 minutes for CP. Blank experiments were also performed following the same procedure except for adding the catalytic material. All experiments were conducted in a photoreactor equipped with ultraviolet LEDs with a wavelength of 385 nm that is further connected to a cooling system at 20 °C. The photocatalytic activity of the materials was preserved for at least six months in which they were stored in the laboratory bench without any special precaution. The concentrations of MB and CP were determined by measuring the maximum absorbance of the solutions at 664 nm for MB and 272 nm for CP. The percentage degradation of MB and CP was calculated at both 30 and 60 minutes, as defined by eqn (1).

$$\%(X) = \frac{C_\mathrm{i} - C_\mathrm{f}}{C_\mathrm{i}} \times 100 \tag{1}$$

The kinetic curves were fitted with a logarithmic curve corresponding to a first-order reaction, defined by eqn (2), and obtaining the kinetic constant k from the slope of the linear fit.

$$\ln C = \ln C_0 - kt \tag{2}$$

In the mechanistic experiments of the MB and CP photodegradation, 5 equivalents of *tert*-butyl alcohol were used as scavengers of hydroxyl radicals ($OH^\bullet$). Finally, the recyclability experiments were performed using the **F-TiO$_2$@1CTF** material during five consecutive catalytic runs (including dye adsorption and photodegradation per each run) for the MB photodegradation. The hybrid material in 10 ppm MB (0.25 mg mL^{-1}) was subjected to one hour of stirring in the dark to facilitate the adsorption of the MB on the hybrid surface. After determining the MB adsorption by UV-visible absorption spectroscopy, it was irradiated with UV light for 50 minutes and the absorbance spectrum of the resulting MB solution was analyzed to determine their photodegradation efficiency. Subsequently, the amount necessary to reach 10 ppm MB concentration was added to carry out the next adsorption and photocatalytic cycle.

Characterization of materials

Morphological characterization of the materials was conducted using a scanning electron microscope (FEI Nova NanoSEM 230 microscope) at 3 keV and a transmission electron microscope JEOL JEM-F200 200 kV equipment. Crystallinity was studied through X-ray diffraction measurements, conducted with a Panalytical Empyrean and Bruker D8 diffractometers at 45 kV and 40 mA, using Cu-Kα radiation (λ = 1.5418 Å). Adsorption–desorption isotherms of nitrogen were measured with a Micromeritics ASAP 2020, applying the Barret–Joyner–Halenda (BJH) model. FT-IR spectroscopy was performed to evaluate the structural features of different materials using a PerkinElmer FT-IR Spectrum 100FTIR spectrometer in transmission mode. The chemical structure of the organic material was analyzed by solid-state ^{13}C-NMR spectroscopy using a Bruker AV 400 WB spectrometer. ^{1}H-NMR spectra were acquired in a Bruker AU III-HD-300 running at 300 MHz. Raman spectroscopy was performed to analyze the features of both materials using a WITec alpha 300R spectrometer with 532 nm laser-excitation, 1 µm spot size, and 0.2 mW power. The optical absorption features were analyzed using UV-Vis Diffuse Reflectance Spectroscopy (DRS) in the range of 250–700 nm by a PerkinElmer LAMBDA 850+ UV/Vis Spectrophotometer equipment. The emission spectra of solid samples were measured using a Fluorescence Spectrofluorometer (PerkinElmer FL 8500) at 320 nm excitation wavelength. The zeta potential analyses were performed at pH 6 using a Particle Analyzer Anton Paar, model Litesizer DLS 500. Absorption spectra of the pollutants were analyzed in an Agilent 8453 UV-visible spectrometer in the range of 190–1100 nm. The electrochemical studies were carried out using a conventional three-electrode cell. The electrode potentials were measured against a saturated Ag/AgCl(s) reference electrode. All the measurements were done in 0.2 mol L^{-1} Na_2SO_4 solution using deionized water. Typically, 4 mg catalyst and 2 mg graphite electrochemical quality (Methrom) were suspended in 1 mL ethanol with 20 µL Nafion solution (5 wt%, Aldrich) to form a homogeneous ink assisted by ultrasound. Then 10 µL of the ink was drop cast onto the surface of glassy carbon by a micropipette and dried under room temperature. Electrochemical impedance spectroscopy (EIS) data were recorded by using a potentiostat/galvanostat with an impedance module with AC signal of 10 mV amplitude in the frequency range between 0.01 Hz and 100 kHz in potentiostatic conditions. Photocurrent was also measured using chronoamperometry technique at 0.6 V *vs.* Ag/AgCl(s) and intermittently illuminated with UV-visible light (Newport 66902 Xenon Lamp, 300 W).

Results and discussion

Preparation and characterization of materials

The quinoline-based building block was obtained following Povarov's and Suzuki–Miyaura's reactions. First, condensation of 4-iodoaniline and 4-iodobenzaldehyde resulted in the formation of imine intermediate that, in the presence of phenylacetylene, undergoes through Povarov's reaction forming the final **Quin-I** (Scheme 1 and Fig. S1 and S2†). Then, a Suzuki–Miyaura's cross-coupling of **Quin-I** with two equivalents 4-cyanophenylboronic acid in the presence of potassium carbonate and $Pd(PPh_3)_4$ as catalyst was performed at 100 °C for 48 hours. The resulting predesigned building block, **Quin-CN** (Scheme 1 and Fig. S3 and S4†), is followed by the cyclotrimerization of nitrile groups in acid media, forming the new **Quin-CTF** material.

The formation of the predesigned **Quin-CTF** material was evaluated by characterizing the three precursor compounds using Fourier Transform Infrared Spectroscopy (FT-IR) and Nuclear Magnetic Resonance (NMR). The corresponding FT-IR spectra of the precursors and the resulting material are displayed in Fig. 1A. The quinoline fragment was successfully formed in the **Quin-I** precursor during Povarov's reaction, confirmed by the presence of characteristic vibrational signals attributed to the quinoline fragment, observed at 1580 and 1600 cm^{-1}, as highlighted in blue.[31] These signals are further preserved in the following reaction steps to form **Quin-CN** and **Quin-CTF**. Additionally, the vibrational band at 461 cm^{-1}, corresponding to the C_aromatic–I fragment, is only detected in the **Quin-I** product. Upon generation of **Quin-CN** *via* Suzuki–Miyaura's cross-coupling, the successful incorporation of benzonitrile groups is evidenced by the appearance of the $\nu(C{\equiv}N)$ stretching band at 2220 cm^{-1} alongside the dis-

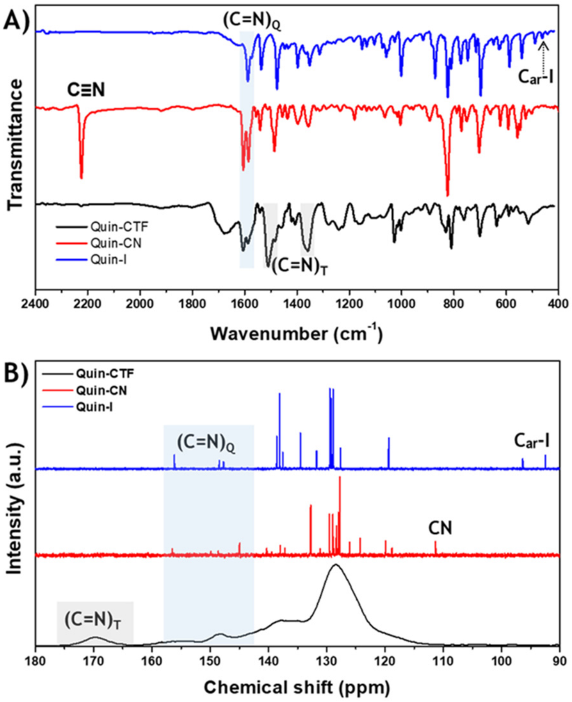

Fig. 1 (A) FT-IR spectra and (B) ^{13}C-NMR spectra of the organic precursors **Quin-I** (blue curves), **Quin-CN** (red curves) and **Quin-CTF** (black curves), highlighting with colored areas the main signals.

appearance of the $\mathrm{C_{aromatic}}$–I signals. In the final product, **Quin-CTF**, the nitrile band at 2220 cm^{-1} disappears, and new signals corresponding to the triazine group appear at 1360 and 1510 cm^{-1}, highlighted in gray.[23] These spectral changes conclusively demonstrate the cyclotrimerization of the building block, confirming the successful formation of the **Quin-CTF** framework.

Further structural confirmation of the organic precursors was obtained through liquid ^{13}C-NMR spectroscopy, and in the case of the **Quin-CTF** material, through cross-polarization magical angle spinning solid-state ^{13}C-CP MAS NMR spectroscopy (Fig. 1B). In agreement with FTIR results, the **Quin-I** precursor presents the signals of the quinoline at 148 and 156 ppm,[31] the $\mathrm{C_{ar}}$–I at 92 and 96 ppm, and the benzene ring carbon at 120–136 ppm. Furthermore, the spectra of the **Quin-CN** precursor preserve the signals of the quinoline and benzene moieties. Importantly, the $\mathrm{C_{ar}}$–I signal disappears while the characteristic signal of nitrile groups appears at 110 ppm, proving its expected chemical structure. Finally, the solid-state ^{13}C-CP MAS NMR spectrum of the **Quin-CTF** material presents the broad signals of the triazine moieties at *ca.* 170 ppm,[23] while the characteristic signal of the nitrile groups disappears. In addition, the aromatic signals are consistent with the presence of quinoline fragments.

Nanoparticles of mesoporous aggregates of 5% fluorine-doped titanium dioxide (**F-TiO$_2$**) were prepared by hydrolysis of titanium(IV) isopropoxide in aqueous HNO$_3$ at pH 2 using a solution of NaF in ultrapure water as a dopant agent with subsequent calcination at 500 °C. **Quin-CTF** was deposited on the surface of this material by simple adsorption in an ethanolic medium. The process involved sonication for 1 hour to ensure homogeneity, followed by magnetic stirring at room temperature for 48 hours. This resulted in the formation of the hybrids **F-TiO$_2$@0.5CTF**, **F-TiO$_2$@1CTF**, and **F-TiO$_2$@2CTF** which contains **Quin-CTF** weight fractions of 0.5, 1 and 2%, respectively. The exceptional sensitivity of Raman spectroscopy to detect the vibrational modes of substances in low amounts was employed to confirm the presence of the **Quin-CTF** in the hybrid materials (Fig. 2). The most prominent Raman band of the **Quin-CTF** appears at 1600 cm^{-1}, which corresponds to the vibrational modes of sp^2-hybridized carbon atoms in the material (C═C and C═N), analogous to the G-band typically associated with graphite.[32,33] In all hybrid samples, the presence of **F-TiO$_2$** was also confirmed by the Raman signals characteristic of the anatase phase, with peaks detected at 134, 386, 509, and 631 cm^{-1}.[34] Furthermore, in the spectrum of the **F-TiO$_2$@0.5CTF** hybrid material, which contains a very low proportion of **Quin-CTF**, its characteristic signal is undetectable. This absence of signal is probable due to the very small amount of **Quin-CTF** in the sample which precludes a clear identification by Raman spectroscopy. In contrast, the Raman spectra of **F-TiO$_2$@1CTF** and **F-TiO$_2$@2CTF** hybrid systems exhibit signals corresponding to the anatase phase of **F-TiO$_2$**, and a second peak attributed to **Quin-CTF** at approximately 1600 cm^{-1}. The intensity of this peak increases proportionally with the amount of **Quin-CTF** in the hybrids, confirming its successful incorporation.

The crystallinity of the materials was determined by X-ray diffraction (Fig. 3 and S5†). The XRD patterns of pristine **F-TiO$_2$** are consistent with Raman results and previously obtained data on similar systems,[35] demonstrating a clear predominance of the anatase crystalline phase. The electronic and textural properties of the anatase favor its photocatalytic behavior.[36] The application of Scherrer's equation[30] results in average crystallite sizes of 11.63 nm for **F-TiO$_2$** and 11.79 nm for **F-TiO$_2$@2CTF**. The preservation of the predominant anatase structure and the similarity in crystallite sizes between **F-TiO$_2$** and the hybrid

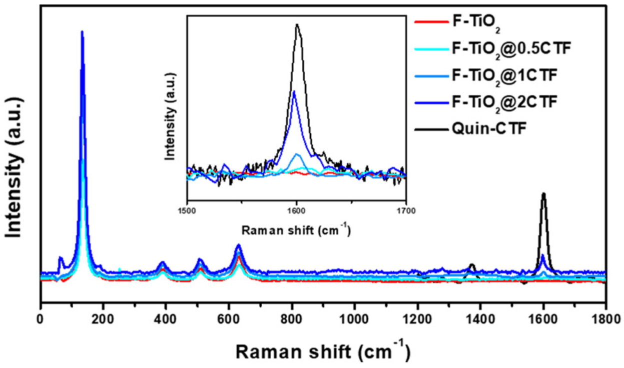

Fig. 2 Raman spectra of **F-TiO$_2$** (red curve), **F-TiO$_2$@CTF** hybrid systems (blue curves), and **Quin-CTF** (black curve) with a zoom in 1500–1800 cm^{-1} showed in the inset.

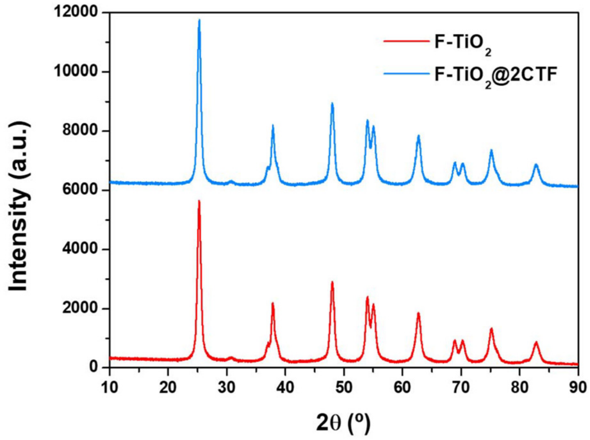

Fig. 3 X-ray diffractograms of **F-TiO$_2$** and **F-TiO$_2$@2CTF** materials.

system **F-TiO$_2$@2CTF** indicate that the functionalization methods do not significantly affect the morphology of the nanoparticles of the base material. Furthermore, X-ray diffraction (XRD) of **Quin-CTF** did not show any diffraction peaks (Fig. S5†), confirming the amorphous nature of the triazine polymer as previously reported for similar materials.[37]

Scanning electron microscopy (SEM) was used for the determination of the morphological characterization of materials. **Quin-CTF** material presents layered microstructure from the stacking of 2D architecture (Fig. 4A) whereas **F-TiO$_2$** exhibits agglomerated nanoparticles (Fig. 4B). The morphology of the **F-TiO$_2$@1CTF** hybrid is similar to that observed for **F-TiO$_2$** (Fig. 4C) which is consistent with layered-CTF covered by titanium dioxide nanoparticles. TEM observations further confirmed the layered nature of the **Quin-CTF** (Fig. 4D). Additionally, the unaltered morphology of the TiO$_2$ nanoparticles was confirmed by the corresponding TEM images of the **F-TiO$_2$** (Fig. 4E) and **F-TiO$_2$@1CTF** (Fig. 4F) systems, which show that the particle size of the nanoparticles remains intact in both cases, with an average size of 12.82 ± 2.31 and 11.91 ± 2.48 nm for, **F-TiO$_2$** and **F-TiO$_2$@1CTF** respectively (Fig. S6†).

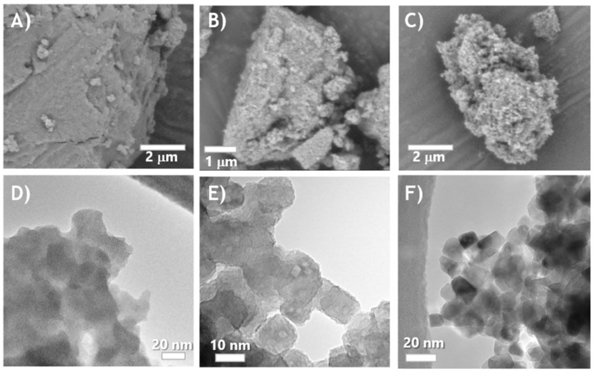

Fig. 4 SEM images of (A) **Quin-CTF**, (B) **F-TiO$_2$** and (C) **F-TiO$_2$@1CTF** samples and TEM images of (D) **Quin-CTF**, (E) **F-TiO$_2$** and (F) **F-TiO$_2$@1CTF** samples.

The optical absorption properties of the synthesized samples were determined using UV-visible diffuse reflectance spectroscopy, as illustrated in Fig. 5A. The absorption spectrum of **F-TiO$_2$** reveals an abrupt absorption increase at around 400 nm which is shifted to lower wavelengths (visible range) in the hybrids and, specifically, in the **Quin-CTF** material. Kubelka–Munk transformed spectra (Fig. 5B) allowed us to estimate the corresponding band gap energies of the materials, resulting in 2.47 eV for the **Quin-CTF** material and 3.14 eV for **F-TiO$_2$**. Furthermore, the small amounts of **Quin-CTF** presented in the hybrid materials improve the optical pro-

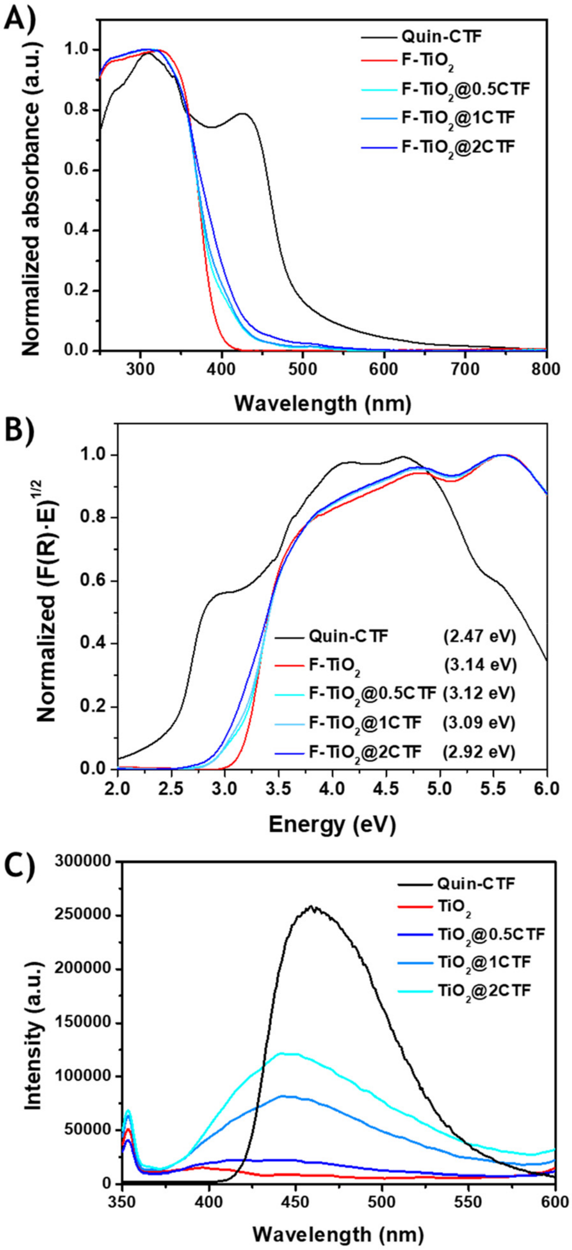

Fig. 5 Diffuse reflectance spectroscopy: (A) absorbance spectra and (B) corresponding Kubelka–Munk plots and (C) fluorescence spectra of the hybrid materials and their counterparts.

perties, leading to redshift in the absorption edge up to 50 nm. Consequently, the band gap energy is reduced with the increase of the CTF content (3.12, 3.09, and 2.92 eV for 0.5, 1 and 2 wt% of CTF, respectively). These results suggest that modification of **F-TiO$_2$** with **Quin-CTF** results in a certain degree of band gap reduction, which is typically expected to enhance photocatalytic activity. Yet, other factors such as the interactions between the photocatalyst and the target contaminant, the surface properties of the materials, and the dynamics of surface reactions, can also play a role in dictating the overall photoactivity of these systems. The solid-state fluorescence emission spectra of the **Quin-CTF** material using an excitation wavelength of 320 nm (Fig. 5C) shows a strong emission band centered at 465 nm. The **F-TiO$_2$@CTF** showed a high fluorescence centered at 445 nm and its intensity depends on the **Quin-CTF** content. These results indicate the correct functionalization of the systems, emphasizing that small amounts of **Quin-CTF** are effectively hybridized with the **F-TiO$_2$**, leading to significant changes in the optoelectronic properties of the resulting hybrid materials.

The most representative material **F-TiO$_2$@1CTF**, together with pristine **F-TiO$_2$** and **Quin-CTF**, were characterized by electrochemical impedance spectroscopy (EIS) in a solution of Na_2SO_4 0.2 M. The Nyquist plot in Fig. 6A and S7† showed a semicircle at high frequencies corresponding to the charge transfer resistance and a straight sloping line at low frequencies attributed to diffusional impedance. The radius of the arc on the Nyquist plot of **F-TiO$_2$@1CTF** sample is smaller than that of the **F-TiO$_2$** counterpart but higher than those of **Quin-CTF**, indicating that charge transfer efficiency was considerably improved after **F-TiO$_2$** functionalization with **Quin-CTF** compound. In addition, photocurrent experiments were measured at constant potential, +0.6 V *vs.* Ag/AgCl for **F-TiO$_2$@1CTF**, **F-TiO$_2$** and **Quin-CTF** (Fig. 6B). All materials exhibit a good response to UV-visible light, being the photocurrent of **F-TiO$_2$@1CTF** significantly higher than that of bare **Quin-CTF** and **F-TiO$_2$**. In particular, photocurrent has increased 29 and 37 nA after irradiation (average of 6 on–off cycles) for **Quin-CTF** and **F-TiO$_2$**, respectively. Interestingly, **F-TiO$_2$@1CTF** shows a higher photoresponse (95 nA), being three times higher than its individual components. These results indicate that hybridization with **F-TiO$_2$** with **Quin-CTF** reduces the charge transfer resistance and increases the photoresponse, suggesting a potential improvement in photocatalytic behavior (*vide infra*).

N_2 adsorption–desorption isotherms (Fig. S8†) were measured for **F-TiO$_2$@1CTF**, **F-TiO$_2$** and **Quin-CTF**. All samples exhibited typical type IV isotherms according to the IUPAC classification, with a small H2 hysteresis loop observed for the **F-TiO$_2$** and hybrid systems **F-TiO$_2$@1CTF**, and H3 hysteresis loop for the **Quin-CTF**.[38] Fig. S8A† shows the physical parameters derived from the nitrogen adsorption isotherms, including BET surface area (S_{BET}), BJH mean pore diameter (D_p) and BJH pore volume (V_p). The BJH pore size distribution resulting from the desorption step of the isotherm (Fig. S8B†) illustrates narrow pore size distributions for pure **F-TiO$_2$** and **F-TiO$_2$@1CTF** hybrid arranged in the range between 10–40 nm in both cases.

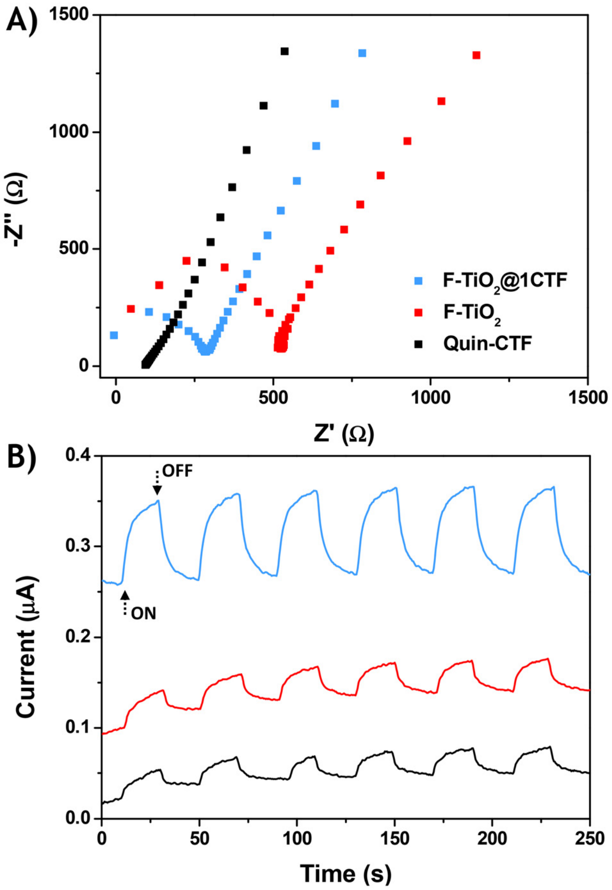

Fig. 6 Electrochemical studies of **F-TiO$_2$**, **F-TiO$_2$@1CTF** and **Quin-CTF** in Na_2SO_4 0.2 M *vs.* Ag/AgCl (3 M KCl). (A) Nyquist plots obtained without applying bias and (B) photocurrent response at a potential of 0.6 V *vs.* Ag/AgCl (3 M KCl) under irradiation with UV-vis light.

Zeta potential measurements were conducted to investigate the materials' behavior in suspension. These measurements were performed using 2.5 mg of the material dispersed in 10 mL of Milli-Q water (H_2O-MQ) at pH 6.0 and 25 °C (Table 1). The data obtained show that the incorporation of **Quin-CTF** leads to a slight increase in the negative value of the zeta potential in the hybrid materials compared to pristine **F-TiO$_2$**. A more negative zeta potential indicates a higher surface charge in absolute terms, which leads to a higher electrostatic repulsion between particles. This improves colloidal stability, essential in applications requiring homo-

Table 1 Zeta potential (ZP) of the studies materials

Materials	Mean zeta potential (mV)
Quin-CTF	−106.22 ± 5.82
F-TiO$_2$	−26.36 ± 3.99
F-TiO$_2$@0.5CTF	−36.02 ± 5.93
F-TiO$_2$@1CTF	−38.17 ± 4.82
F-TiO$_2$@2CTF	−40.57 ± 4.64

geneous dispersions and large surface areas such as water treatment, coatings, and photocatalytic systems.

From a macroscopic perspective (Fig. S9†), a significant enhancement in the dispersibility of **F-TiO$_2$** systems is observed with the presence of surface-functionalized CTF. The incorporation of CTF improves dispersion due to its surface characteristics, which help reduce the attractive forces between **F-TiO$_2$** nanoparticles, thereby enhancing their overall performance in terms of activity and efficiency.

Application of the materials for the removal of pollutants in water

The photocatalytic activity of the hybrid materials and their counterparts was studied towards the degradation of two selected organic compounds from common dyes and pharmaceuticals in water, MB and CP. First, we evaluated the adsorption capabilities of the catalytic materials (0.25 mg mL^{-1}) in MB aqueous solution (10 ppm) by analyzing the concentration of the dye solution through UV-visible absorption spectroscopy after one hour of stirring in the absence of light. Adsorption tests (Fig. S10A and E†) showed that **F-TiO$_2$** and hybrid materials have a considerable affinity for MB adsorbing 51–65%, whereas **Quin-CTF** demonstrated low adsorption capacities (17%). All materials showed a limited affinity for CP, adsorbing less than 4% (Fig. S10B and F†). Then, photodegradation tests were conducted under the same conditions and using a LED light source of 385 nm for 50 and 30 minutes in the case of MB and CP, respectively. As a control experiment, blank solutions without material were irradiated under identical conditions, presenting a photolysis of 20% for the MB and 5% for the CP.

The results of the MB photocatalytic tests show that all the materials exhibit significant degradation (Fig. S10C and E†), achieving >99% degradation when using the hybrid materials. Similarly, the hybrids present a significant photodegradation of the CP antibiotic, higher than 85% in 30 minutes (Fig. S10D and F†). To determine which material showed the most promising photocatalytic behavior, a comparative kinetic study was performed by measuring the UV-visible absorbance spectra of the pollutants (Fig. S11 and S12†) at different time intervals. The results of the kinetic studies depicted first-order kinetics for the photodegradation of both pollutants (Fig. 7A and B), which allowed the calculation of the photocatalytic degradation kinetic constants (Fig. 7C). The kinetic constant of the MB photodegradation is four times higher in the hybrids than when using the pure **F-TiO$_2$** and double than that of the **Quin-CTF**. Examination of the data available in the literature of MB using TiO$_2$-based catalysts shows that activity of **F-TiO$_2$@1CTF** is in the state of the art (Table S1†). In the case of the CP, hybrid materials also present higher kinetic constant values than pure **F-TiO$_2$** but are very similar to the **Quin-CTF**. However, in contrast to the progressive CP photodegradation observed for pure **F-TiO$_2$** or hybrid materials, the kinetics of the **Quin-CTF** material (Fig. S12A†) show that after 10 minutes of photodegradation tests, the solution contains slightly different spectra that does not evolve with reaction time. We reused the same material to prove the perseverance of its photocatalytic activity, and the same results were reproduced, confirming that **Quin-CTF** material preserves its photocatalytic activity (Fig. S13A†).

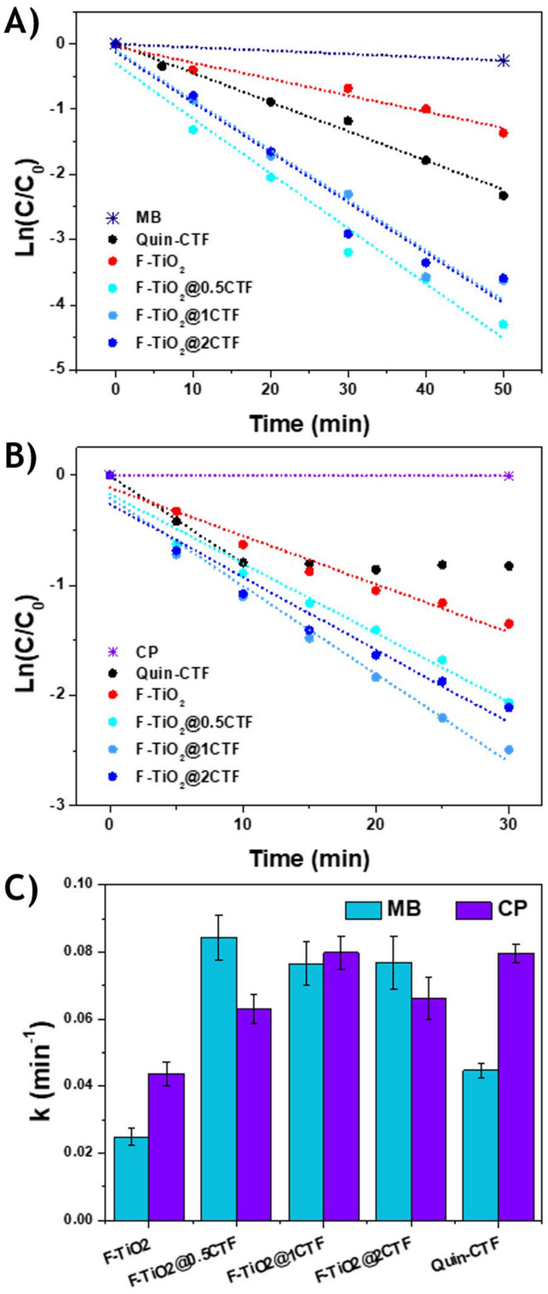

Fig. 7 Kinetic experiments for the photodegradation of (A) MB and (B) CP using the **Quin-CTF** (black), **F-TiO$_2$** (red), **F-TiO$_2$@CTF** (blue) materials and respective control. (C) Bar diagram with the kinetic constant calculated from the fit of the kinetic experiments.

Additionally, we performed photocatalytic experiments changing the CP concentration from 20 ppm to 10 and to 40 ppm and observed the same effect, namely, absorption decreases to half of the initial absorption, independently of the pollutant solution concentration (Fig. S13B†). These experiments suggest that **Quin-CTF** can rapidly degrade the CP to a product that presents absorption in the UV range, which is different from those obtained with **F-TiO$_2$** or **F-TiO$_2$@CTF** hybrid photocatalysts. Further insights were obtained by electrospray analysis of the reaction crudes after 30 minutes of the photocatalytic reaction (Fig. S14†). For **F-TiO$_2$** and **Quin-CTF**, several species at 362, 356, 334, 285, and 263 *m*/*z*, were observed, which correspond to the piperazine ring open pathway.[39] These detected products (Fig. S15†) contain aromatic fragments which is consistent with the final UV-visible absorption spectra in the mixtures. Interestingly, while these fragments are further degraded when **F-TiO$_2$** is used, they remain stable when **Quin-CTF** is employed as photocatalyst. In contrast, for **F-TiO$_2$@1CTF** hybrid material, fragments from CP degradation were not identified, which is consistent with the null absorption in the UV-visible spectra after 30 minutes of reaction.

Typically, photooxidative processes catalyzed by TiO$_2$ work *via* the formation of hydroxyl radicals.[40] In order to assess the involvement of such reactive oxidative species when **F-TiO$_2$**, **Quin-CTF** and **F-TiO$_2$@1CTF**, we performed photocatalytic tests using 5 equivalents of *tert*-butyl alcohol as a hydroxyl radical (OH$^\bullet$) scavenger. As expected, the results showed that for the **F-TiO$_2$** material, *tert*-butyl alcohol acts as a quencher of the MB degradation, reducing the reaction conversion by 69% and giving evidence of hydroxyl radical production as an oxidant species (Fig. 8A and S16†). However, the photodegradation of MB for **Quin-CTF** and **F-TiO$_2$@1CTF** hybrid materials has been only slightly altered in the presence of *tert*-butyl alcohol. In addition, quenching experiments with the CP pollutant were also studied (Fig. 8B and S17†). Similarly, in the presence of *tert*-butyl alcohol, the CP photodegradation was only slightly reduced in the **Quin-CTF** and **F-TiO$_2$@1CTF** hybrid materials whereas its photodegradation conversion decreased by 28% in the **F-TiO$_2$**. The effect of adding *tert*-butyl alcohol is less prominent when CP was studied than in the MB essays. This reduced effect is attributed to CP's faster photodegradation kinetics that makes it a more competent substrate *versus* *tert*-butyl alcohol. Overall, these results indicate that while **F-TiO$_2$** works *via* the formation of hydroxyl radical species, as typically observed in TiO$_2$ materials,[40] for **Quin-CTF** and **F-TiO$_2$@1CTF**, such intermediate does not seem to be the main oxidant involved in pollutant degradation. To expand the mechanistic insights, we performed the photocatalytic tests for the MB degradation using benzoquinone (BQ) and 1,4 diazabicyclo[2.2.2]octane (DABCO) as scavengers for O$_2^{\bullet-}$ and ^{1}O$_2$, respectively. Owing the lower kinetics of MB degradation, we focused on this dye to study the effect of these other scavengers when **F-TiO$_2$**, **Quin-CTF**, and **F-TiO$_2$@1CTF** materials are used as photocatalyst (Fig. S16†). For the **F-TiO$_2$** sample, all scavengers (*tert*-butyl alcohol, benzoquinone and DABCO) completely quench the photodegradation of MB. This observation suggests that all reactive oxygen species are involved in the reaction pathway, which appears to be crosslinked.[41] In the case of **Quin-CTF** material, both benzoquinone and DABCO partially quench the reaction involving the O$_2^{\bullet-}$ and ^{1}O$_2$ species in the photodegradation mechanism. However, for the **F-TiO$_2$@1CTF**, benzoquinone is the most effective quencher, suggesting that the preferred pathway occurs involving O$_2^{\bullet-}$ species. Interestingly, the hybrid material, which is the most active photocatalyst, shows a more selective ROS generation.

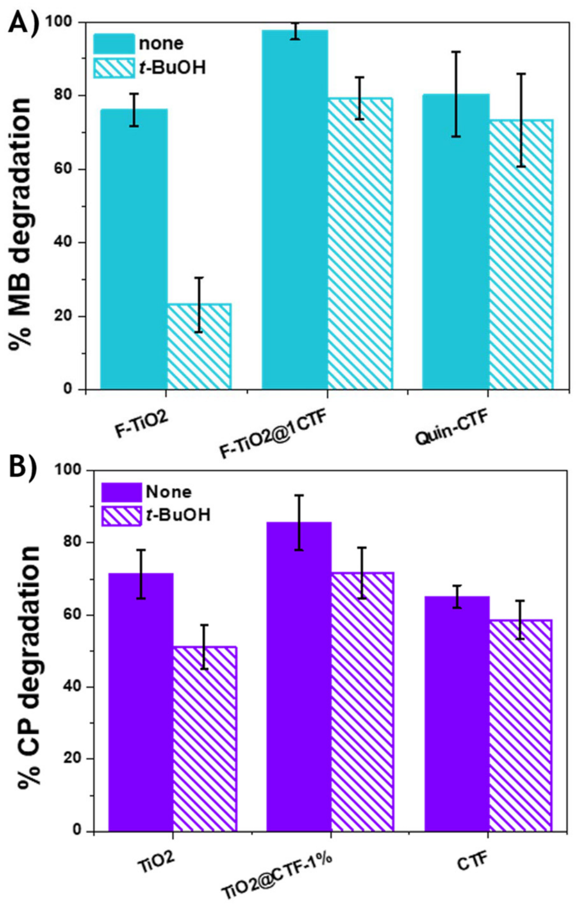

Fig. 8 Mechanistic essays using *tert*-butanol as hydroxyl radical scavenger on the photocatalytic degradation of (A) MB and (B) CP using **F-TiO$_2$**, **Quin-CTF** and **F-TiO$_2$@1CTF** photocatalysts.

A deeper mechanistic understanding of MB photodegradation was obtained from the analysis of UV-vis spectra at 0 and 50 minutes of photodegradation (Fig. S18†). Initially, after adsorption procedure using **F-TiO$_2$**, **Quin-CTF**, and **F-TiO$_2$@1CTF** (at $t = 0$), deconvolution of MB signals shows in all cases similar spectra with two fitted Gaussian peaks at 664 and 622 nm. These two signals are attributed to monomer and dimer species of MB, respectively.[42] After 50 minutes of photodegradation, small shifts of 7 and 10 nm were observed in the maximum absorbance peaks of residual MB for the **Quin-CTF** and **F-TiO$_2$** materials, respectively. However, a blueshift of around 40 nm occurred for the **F-TiO$_2$@1CTF** sample. This enhanced blueshift is related to the *N*-demethylation of MB.[43]

Overall, **F-TiO$_2$@1CTF** hybrid material, which is the most efficient photocatalyst, selectively activates oxygen to form superoxide radical. Furthermore, it decomposes MB though consecutive *N*-demethylation in a more extensive way than pristine materials (Fig. S19†). In addition, this hybrid photocatalyst can decompose CP into smaller fragments than those obtained with individual components (Fig. 9). Taken together, these data illustrate the uniqueness of **F-TiO$_2$@1CTF** as a photocatalyst. Considering the small amounts of **Quin-CTF** in the **F-TiO$_2$@1CTF** hybrid, the differences in its photocatalytic behavior with respect to that of pristine titanium dioxide are a remarkable example of a synergistic effect in the hybrid material.

Finally, recyclability tests were performed using **F-TiO$_2$@1CTF** and MB as the model pollutant. In these essays, a dispersion of the hybrid material in 10 ppm MB (0.25 mg mL^{-1}) was subjected to irradiation with UV light for 50 minutes and the absorbance spectrum of the resulting MB solution was analyzed to determine their photodegradation efficiency. Subsequently, the amount necessary to reach 10 ppm MB concentration was further added to perform the next photocatalytic cycle. The results of this experiment show the effective recyclability of the hybrid material whose photocatalytic properties are preserved during the whole recyclability test, although a 30% loss in catalytic activity is observed after five consecutive cycles (Fig. 10 and S20†).

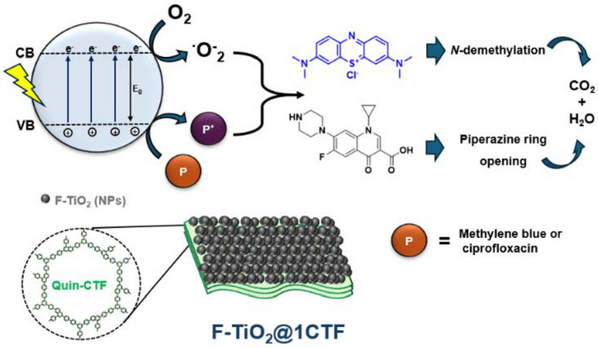

Fig. 9 Schematic representation of the mechanism for the photodegradation of pollutant in water using the **F-TiO$_2$@1CTF** photocatalyst.

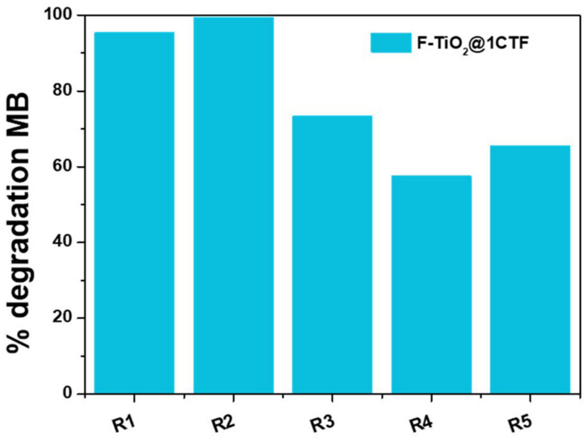

Fig. 10 Recyclability essay for the photocatalytic degradation of MB using **F-TiO$_2$@1CTF** photocatalyst.

Conclusions

In this work, we successfully synthesized a novel quinoline-based covalent triazine framework (**Quin-CTF**) that has been combined with fluorine-doped titanium dioxide to form **F-TiO$_2$@CTF** hybrid materials, which have shown attractive photocatalytic properties. This study highlights a strategic approach to enhance the photocatalytic performance of TiO$_2$ through hybridization with CTFs, addressing critical challenges in removing persistent water pollutants such as MB and CP. The new hybrid materials exhibited new optical absorption and emission properties, attributed to the synergistic interaction between the structural and electronic characteristics of both components. These changes result in significantly superior photocatalytic activity of **F-TiO$_2$@CTF** hybrids compared to pristine materials, achieving near-complete removal (>99%) of MB and substantial degradation (>85%) of CP within short irradiation periods. Surprisingly, the small amount of **Quin-CTF** in **F-TiO$_2$@1CTF** hybrid system (1 wt%) has a significant effect not only on the catalytic activity but also on the reaction pathways of the photodegradation of pollutants. While **F-TiO$_2$** works essentially *via* the formation of hydroxyl radicals, in **Quin-CTF** and **F-TiO$_2$@1CTF** hybrid, the involvement of such radical species has a minor relevance in its photocatalytic activity. Furthermore, these hybrid materials demonstrated excellent reusability, maintaining high photocatalytic efficiency over multiple cycles, which underscores their potential for practical water treatment applications. Taken together, this work demonstrates that the photocatalytic performance of low-cost TiO$_2$ materials can be further enhanced with a very small amount of pre-designed photoactive organic materials improving their potential in environmental remediation. Overall, these findings contribute to sustainable and cost-effective technologies for mitigating water pollution, helping in the preservation and remediation of aquatic ecosystems, promoting cleaner and more sustainable water management solutions. Building on these findings, our current focus is on advancing studies on new TiO$_2$@CTF hybrid systems to explore how the incorporation of the organic compounds within the inorganic materials could lead to strategic materials' changes that may alter their electronic behavior. This approach aims to develop next generation memristor devices with enhanced performance, with the potential of memory storage, neuromorphic computing, and reconfigurable logic circuits in the near future.

Author contributions

Conceptualization: MD-S, SG-R, and RM-B. Synthesis and characterization: AM, MS-F, ML, VC and MD-S.

Electrochemical studies: IH. Photocatalytic studies: AM, MS-F, ML and VC. Writing, original draft preparation, and editing: AM, MS-F, MD-S, SG-R, and RM-B. Supervision: AM, MS-F, MD-S, SG-R and RM-B.

Data availability

The data supporting this article have been included as part of the ESI,† which includes materials characterisation including FT.IR, NMR, PXRD, porosimetry, and UV-visible spectra of photocatalytic studies. Metadata for this article is available *via* the e-cienciaDatos (**https://edatos.consorciomadrono.es/**) repository.

Conflicts of interest

There are no conflicts to declare.

Acknowledgements

RM-B acknowledges that this research received funding through the Spanish Ministry of Science and Innovation MCIN/AEI/FEDER (10.13039/501100011033) through the project PID2022-141016OB-I00 *via* Proyectos de Generación de Conocimiento 2022. SG-R would like to thank funding from the research project PID2022-136417NB-I00 financed by AEI-Ministerio de Ciencia, Innovación y Universidades MCIU/ AEI/10.13039/501100011033/ and "ERDF A way of making Europe" and from the research project PDC2023-145884-I00 finance by AEI-Ministerio de Ciencia, Innovación y Universidades MICIU/AEI /10.13039/501100011033 and the European Union Next GenerationEU/ PRTR. AM acknowledges the Spanish Government and the Funds Next Generation of the European Union through the grant Maria Zambrano-UAM (CA3/RSUE/2021-00648). MS-F thanks Ministerio de Ciencia e Innovación for a FPI contract (PRE2020-092295).

References

1 N. A. Khan, E. A. López-Maldonado, A. Majumder, S. Singh, R. Varshney, J. R. López, P. F. Méndez, P. C. Ramamurthy, M. A. Khan, A. H. Khan, N. M. Mubarak, W. Amhad, S. Z. M. Shamshuddin and I. H. Aljundi, *Chemosphere*, 2023, **344**, 140264.

2 J. Wang and S. Wang, *Chem. Eng. J.*, 2020, **401**, 126158.

3 J. Zhang, S. Yang, K. Zhou, J. Zhao, J. Wang, N. Li, Y. Wang, Y. Li and T. E, *Chem. Eng. J.*, 2024, **491**, 151985.

4 M. Zeshan, I. A. Bhatti, M. Mohsin, M. Iqbal, N. Amjed, J. Nisar, N. AlMasoud and T. S. Alomar, *Chemosphere*, 2022, **300**, 134525.

5 A. Balakrishnan, S. Appunni, M. Chinthala and D. N. Vo, *Environ. Chem. Lett.*, 2022, **20**, 3071–3098.

6 K. P. Gopinath, N. V. Madhav, A. Krishnan, R. Malolan and G. Rangarajan, *J. Environ. Manage.*, 2020, **270**, 110906.

7 J.-P. Jeon, D. H. Kweon, B. J. Jang, M. J. Ju and J.-B. Baek, *Adv. Sustainable Syst.*, 2020, **4**, 2000197.

8 M. Zulfiqar, S. Sufian, A. Bahadar, N. Lashari, N. E. Rabat and N. Mansor, *J. Cleaner Prod.*, 2021, **317**, 128354.

9 S.-M. Wu and P. Schmuki, *Energy Technol.*, 2023, **11**, 2300052.

10 A. Moya, A. Cherevan, S. Marchesan, P. Gebhardt, M. Prato, D. Eder and J. J. Vilatela, *Appl. Catal., B*, 2015, **179**, 574–582.

11 A. Moya, M. Barawi, B. Alemán, P. Zeller, M. Amati, A. Monreal-Bernal, L. Gregoratti, V. A. de la Peña O'Shea and J. J. Vilatela, *Appl. Catal., B*, 2020, **268**, 118613.

12 M. Díaz-Sánchez, P. Reñones, I. Mena-Palomo, E. López-Collazo, F. Fresno, F. E. Oropeza, S. Prashar, V. A. de la Peña O'Shea and S. Gómez-Ruiz, *Appl. Catal., A*, 2021, **613**, 118029.

13 J. Yu, W. Wang, B. Cheng and B.-L. Su, *J. Phys. Chem. C*, 2009, **113**, 6743–6750.

14 H. Park and W. Choi, *J. Phys. Chem. B*, 2004, **108**, 4086–4093.

15 E. M. Samsudin, S. B. A. Hamid, J. C. Juan, W. J. Basirun, A. E. Kandjani and S. K. Bhargava, *Appl. Surf. Sci.*, 2016, **365**, 57–68.

16 M. Díaz-Sánchez, R. N. Murgu, D. Díaz-García, J. M. Méndez-Arriaga, S. Prashar, B. Urbán, J. Pinkas, M. Lamač, M. Horáček and S. Gómez-Ruiz, *Adv. Sustainable Syst.*, 2021, 2000298.

17 W.-J. Ong, L.-L. Tan, S.-P. Chai, S.-T. Yong and A. R. Mohamed, *Nanoscale*, 2014, **6**, 1946–2008.

18 M. V. Dozzi and E. Selli, *Catalysts*, 2013, **3**, 455–485.

19 I. J. Gómez, M. Díaz-Sánchez, N. Pizúrová, L. Zajíčková, S. Prashar and S. Gómez-Ruiz, *J. Photochem. Photobiol., A*, 2023, **443**, 114875.

20 M. Ehtisham Khan, *Nanoscale Adv.*, 2021, **3**, 1887–1900.

21 H. R. Abuzeid, A. F. M. El-Mahdy and S.-W. Kuo, *Giant*, 2021, **6**, 100054.

22 M. Liu, L. Guo, S. Jin and B. Tan, *J. Mater. Chem. A*, 2019, **7**, 5153–5172.

23 A. López-Magano, N. Salaverri, L. Marzo, R. Mas-Ballesté and J. Alemán, *Appl. Catal., B*, 2022, **317**, 121791.

24 G. Lu, X. Huang, Z. Wu, Y. Li, L. Xing, H. Gao, W. Dong and G. Wang, *Appl. Surf. Sci.*, 2019, **493**, 551–560.

25 L. Zhou, Z. Huang, H. Zhang, H. Gao, J. Tang and X. Yao, *ChemCatChem*, 2023, **15**, e202300414.

26 Y. Zhang and S. Jin, *Polymers*, 2019, **11**, 31.

27 X. Chao, Y. Xu, H. Chen, D. Feng, J. Hu and Y. Yu, *RSC Adv.*, 2021, **11**, 6943–6951.

28 A. López-Magano, R. Mas-Ballesté and J. Alemán, *Adv. Sustainable Syst.*, 2022, **6**, 2100409.

29 G. Accorsi, A. Listorti, K. Yoosaf and N. Armaroli, *Chem. Soc. Rev.*, 2009, **38**, 1690–1700.

30 M. Díaz-Sánchez, I. Hernández-Benítez, D. Díaz-García, S. Prashar and S. Gómez-Ruiz, *Catal. Commun.*, 2022, **169**, 106477.

31 C.-J. Wu, M.-Z. Shao, J.-L. Kan, W.-J. Liang, T.-R. Li, L.-J. Niu, H.-J. Wang, Y. Geng and Y.-B. Dong, *ACS Mater. Lett.*, 2024, **6**, 5016–5022.

32 A. Moya, N. Kemnade, M. R. Osorio, A. Cherevan, D. Granados, D. Eder and J. J. Vilatela, *J. Mater. Chem. A*, 2017, **5**, 24695–24706.

33 A. Moya, M. Hernando-Pérez, M. Pérez-Illana, C. San Martín, J. Gómez-Herrero, J. Alemán, R. Mas-Ballesté and P. J. de Pablo, *Nanoscale*, 2020, **12**, 1128–1137.

34 A. Saha, A. Moya, A. Kahnt, D. Iglesias, S. Marchesan, R. Wannemacher, M. Prato, J. J. Vilatela and D. M. Guldi, *Nanoscale*, 2017, **9**, 7911–7921.

35 S. Lázaro-Navas, S. Prashar, M. Fajardo and S. Gómez-Ruiz, *J. Nanopart. Res.*, 2015, **17**, 94.

36 J. Zhang, P. Zhou, J. Liu and J. Yu, *Phys. Chem. Chem. Phys.*, 2014, **16**, 20382–20386.

37 A. López-Magano, N. Salaverri, L. Marzo, R. Mas-Ballesté and J. Alemán, *Appl. Catal., B*, 2022, **317**, 121791.

38 M. Thommes, K. Kaneko, A. V. Neimark, J. P. Olivier, F. Rodriguez-Reinoso, J. Rouquerol and K. S. W. Sing, *Pure Appl. Chem.*, 2015, **87**, 1051–1069.

39 C. Hu, M. Chen, L. Wang, Y. Ding, Q. Li, X. Li and J. Deng, *Chemosphere*, 2023, **336**, 139202.

40 J. Zhang and Y. Nosaka, *J. Phys. Chem. C*, 2014, **118**, 10824–10832.

41 T. Daimon, T. Hirakawa, M. Kitazawa, J. Suetake and Y. Nosaka, *Appl. Catal., A*, 2008, **340**, 169–175.

42 S. Y. Lim, C. Hedrich, L. Jiang, C. S. Law, M. Chirumamilla, A. D. Abell, R. H. Blick, R. Zierold and A. Santos, *ACS Catal.*, 2021, **11**, 12947–12962.

43 T. Zhang, T. Oyama, A. Aoshima, H. Hidaka, J. Zhao and N. Serpone, *J. Photochem. Photobiol., A*, 2001, **140**, 163–172.